Reconstitution of Contractile Actomyosin Bundles

Todd Thoresen,[†] Martin Lenz,[†‡] and Margaret L. Gardel[†‡*]
[†]Institute for Biophysical Dynamics and [‡]James Franck Institute and Department of Physics, University of Chicago, Chicago, Illinois

ABSTRACT   Contractile actomyosin bundles are critical for numerous aspects of muscle and nonmuscle cell physiology. Due to the varying composition and structure of actomyosin bundles in vivo, the minimal requirements for their contraction remain unclear. Here, we demonstrate that actin filaments and filaments of smooth muscle myosin motors can self-assemble into bundles with contractile elements that efficiently transmit actomyosin forces to cellular length scales. The contractile and force-generating potential of these minimal actomyosin bundles is sharply sensitive to the myosin density. Above a critical myosin density, these bundles are contractile and generate large tensile forces. Below this threshold, insufficient cross-linking of F-actin by myosin thick filaments prevents efficient force transmission and can result in rapid bundle disintegration. For contractile bundles, the rate of contraction decreases as forces build and stalls under loads of ~0.5 nN. The dependence of contraction speed and stall force on bundle length is consistent with bundle contraction occurring by several contractile elements connected in series. Thus, contraction in reconstituted actomyosin bundles captures essential biophysical characteristics of myofibrils while lacking numerous molecular constituents and structural signatures of sarcomeres. These results provide insight into nonsarcomeric mechanisms of actomyosin contraction found in smooth muscle and nonmuscle cells.

INTRODUCTION

Thick filaments of myosin motors and filamentous actin (F-actin) form the basis of the actomyosin cytoskeleton, which is essential for contraction and force generation in nonmuscle and muscle cells (1–4). Actomyosin networks and bundles of varied compositions and structures are used in diverse physiological processes including muscle contraction (4,5), cell migration (6,7), and cell division (8,9). Significant progress has been made in understanding the mechanisms of force generation and translocation at the scale of individual myosin motors (10,11). However, knowledge of how actomyosin interactions at the molecular level are transmitted to cellular length scales is essential for developing physical models of cellular mechanics.

In striated muscle, force transmission from the molecular to tissue level is well understood (11–14). Within these tissues, myofibrils consist of a series of contractile elements, termed sarcomeres, which form a well-defined, periodic structure on micrometer length scales (12,15). Sarcomeres consist of bipolar myosin thick filaments bound to F-actin of organized polarity and uniform length. The F-actin pointed ends are oriented toward the central bare zone of the thick filament such that motor-mediated F-actin translocation results in contraction, as described by the sliding filament theory (16). At the F-actin barbed ends, passive cross-linking proteins (e.g., α-actinin) serve to link sarcomeres in series (12,15). The exquisite organization of sarcomeres has facilitated our understanding of force transmission in striated muscle. However, there are numerous types of contractile actomyosin bundles in smooth and nonmuscle cells that lack sarcomeric organization (7,9,17–19). In these

nonsarcomeric actomyosin bundles, the underlying mechanisms of contraction and the roles of passive cross-linking proteins are not well understood.

Contraction of actomyosin assemblies in vitro is traditionally studied by polymerizing F-actin in the presence of myosin thick filaments and then assessing the extent of network contraction and force generation at length scales ranging from 100 μm to 10 cm (20–26). Although early work indicated that mixtures of highly concentrated F-actin and myosin contract and generate force (21), it was later shown that these behaviors were not consistent with myosin mechanochemistry and were likely dominated by contaminating factors (27). More recent experiments indicate that passive F-actin cross-linking proteins, such as α-actinin or filamin, are required to facilitate network contraction (23–26). Thus, it is widely believed that myosin filaments alone are insufficient to elicit contraction of actin bundles on cellular length scales.

Contrary to these expectations, we show that a high density of smooth muscle myosin thick filaments is sufficient to elicit contraction of actomyosin bundles in the absence of passive cross-linking proteins. As the myosin density is decreased, we observe first a regime where F-actin bundles are stabilized by myosin cross-links, but no contraction occurs. When myosin density is decreased further, actin bundles are unstable. In contractile bundles, the rate of contraction is load dependent and stalls under forces of ~0.5 nN. This stall force is independent of bundle length. Under low loads, the contraction rate is proportional to bundle length and increases with the density of myosin filaments. These data are consistent with bundle contraction occurring by a series of independent contractile elements. Thus, bundles comprised solely of myosin thick filaments and F-actin spontaneously assemble into linear arrays of

contractile elements that capture the essential biophysical properties of striated myofibrils, although lacking their apparent microstructure and many of their components.

RESULTS

Templated assembly of tethered actomyosin bundles

To template assembly of tethered actomyosin bundles, F-actin asters are formed by decorating neutravidin beads bound to a coverslip with biotinylated, Alexa 568-phalloidin-stabilized F-actin with a mean length of ~6 μm (Fig. 1, a and b, see also Fig. S3, a and b, and Movie S1 in the Supporting Material). Because biotinylated actin is randomly incorporated into F-actin, free F-actin ends emanating from beads (asterisks, Fig. 1 b) are likely of random polarity. A dilute background of free F-actin remains after wash steps.

Thick filaments of Oregon Green (OG)-labeled, smooth muscle myosin with a mean length of ~360 nm are prepared (Fig. S1 and Fig. S3, d and e), diluted in Assay Buffer and perfused into the flow chamber (Fig. 1 a). Because the Assay Buffer contains no nucleotides (NN), the myosin heads are bound with high affinity to F-actin either in rigor or with ADP (28). Over a period of 30 min, actomyosin bundles form (Fig. 1 c, Fig. S2 d, Movie S2). Bundles are largely confined to the coverslip vicinity and elevated from the surface by ~2–4 μm (Fig. S2 e). After bundle formation, myosin remaining in solution is removed by perfusion of Assay Buffer.

The bundle lengths vary widely from 5 to >50 μm, significantly longer than individual F-actin, indicating that F-actin in solution is used to assemble bundles. Bundles often branch and connections between bundles can exist far away from the beads (Fig. 1 c). The variations of both myosin and actin intensity along the bundle contour are, on average, 10% that of the mean intensity (Fig. 1 d). Thus, there are no periodic myosin bands indicating sarcomeric organization (29) within the bundle. Using quantitative fluorescence microscopy, we estimate ~4 F-actin per bundle cross section (Fig. 1 e).

The bundle composition can be altered by varying the myosin concentration from 0.1 μM to 1 μM. Strikingly, the number of F-actin per bundle cross section is independent of myosin concentration (Fig. 1 e). Using quantitative fluorescence microscopy (Fig. S4), we determine that the mole ratio of myosin heavy chains to actin within bundles, $R_{M:A}$, changes from 0.03 to ~2 for bundles formed with 0.1 μM and 1 μM myosin, respectively (Fig. 1 f). Values of $R_{M:A}$ obtained from imaging are consistent with those obtained from densitometry measurements (Fig. 1 f). Because the quantity of actin within bundles does not change, $R_{M:A}$ is also a good measure of the absolute density of myosin per bundle length.

Bundles within a large range of $R_{M:A}$ (0.44–1.9) have qualitatively similar morphologies in the presence of Assay Buffer (top row, Fig. 2 a). They are curved, branched, and fluctuate significantly. For bundles tethered at both ends, the variance of the bundle position in the transverse direction, u_{peak}, (Fig. 1 d) provides a measure of the degree of bundle flexibility and does not change significantly as
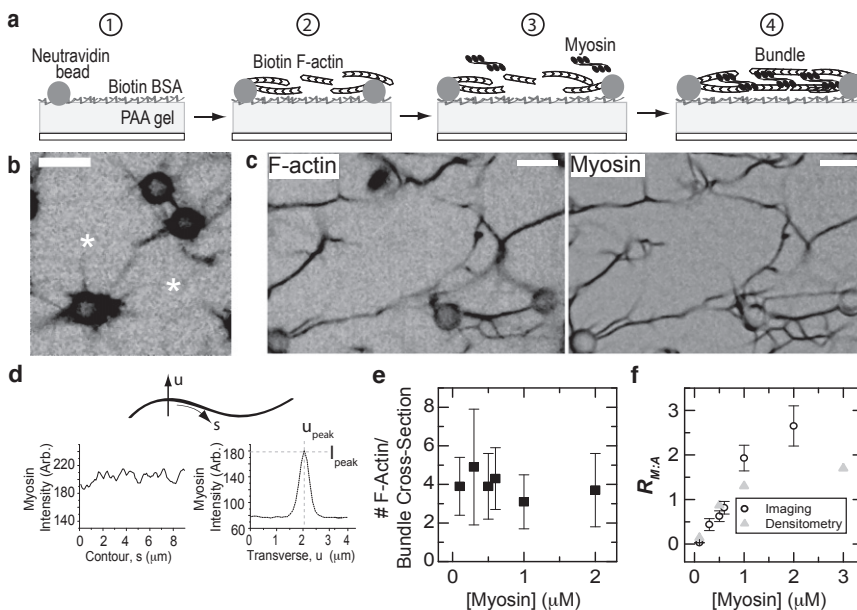

FIGURE 1 Templated assembly of tethered actomyosin bundles. (a) Schematic illustrating the sequential process used for templated bundle assembly (1). Biotinylated-bovine serum albumin is coupled to the surface of a PAA gel affixed to a glass coverslip. Neutravidin beads (gray circles) bind to the biotinylated-bovine serum albumin (2). Biotinylated F-actin (chevrons) is introduced and bind to beads. A dilute suspension of F-actin remains (3). Myosin thick filaments suspended in nucleotide free Assay buffer (black) are introduced (4). F-actin cross-linking by myosin filaments mediates bundle formation. (b) Inverted contrast image of F-actin asters visualized with Alexa 568-phalloidin before myosin perfusion. Dark circles are F-actin-coated beads. Asterisks indicate free F-actin ends. Scale bar is 5 μm; see Movie S1. (c) Inverted contrast images of F-actin visualized with Alexa 568-phalloidin (left) and OG-labeled myosin (right) illustrating network of bundles formed after 30 min incubation of F-actin asters with myosin thick filaments. Scale bar is 5 μm. (d) Schematic diagram illustrating transverse, u, and longitudinal, s, directions along a bundle. Plots of OG-myosin intensities in transverse and longitudinal line scans are shown below. For transverse line scans, the location, u_{peak}, and intensity, I_{peak}, of the peak are determined. (e) Number of F-actin per bundle cross section as a function of myosin concentration. Error bars indicate standard deviations, (n = 7–28 bundles for each data point). (f) The mole ratio of myosin heavy chains to actin in the bundles determined from quantitative fluorescence imaging (triangles) and densitometry (open circles) as a function of myosin concentration. Error bars for imaging indicate standard error (n = 20 bundles for each data point).
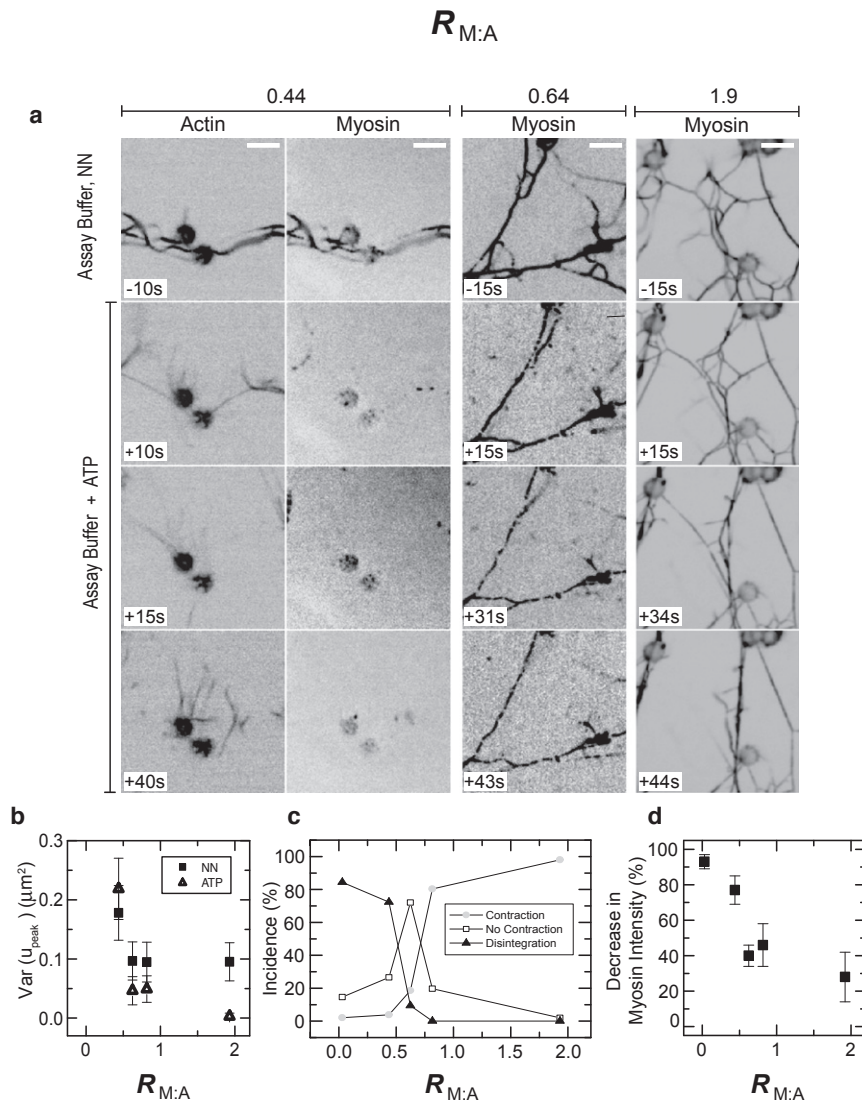
FIGURE 2 A critical myosin density is required to stabilize bundles and facilitate contraction. (*a*) Inverted contrast images of OG-myosin in bundles formed with $R_{M:A} = 0.44$, 0.64 and 1.9 in nucleotide-free (NN) Assay buffer (*top row*) and at three times after addition of Assay buffer containing 1 mM ($R_{M:A} = 0.44$ or 0.64) or 0.1 mM ($R_{M:A} = 1.9$) ATP (*bottom rows*). All times are indicated in seconds either before (*negative times*) or after (*positive times*) ATP addition. For $R_{M:A} = 0.44$, inverted contrast images of F-actin, visualized with Alexa 568-phalloidin, is also shown to illustrate the dissociation of F-actin from bundles and the re-appearance of F-actin asters by +40s (see Movie S3). Scale bars are 5 μm. (*b*) Amplitude of transverse fluctuations of bundle contour, measured by the variance of the bundle midpoint position in direction normal to the bundle contour, u_{peak}, as a function of $R_{M:A}$ in both nucleotide-free (*solid black squares*, NN) or 1 mM ATP (*open triangles*, ATP) conditions. Data shown are mean $\pm$ SE. ($n = 12–15$ bundles for all conditions). (*c*) Incidence, reported as percentage, of the states observed after ATP perfusion: contraction, bundles remain stable without contraction (no contraction) or bundles disintegrate as a function of $R_{M:A}$ ($n > 48$ bundles for each data point). Data points obtained within 1 min of ATP perfusion. (*d*) Percent decrease in myosin intensity after the first 45 s of ATP addition. Data shown are mean $\pm$ SD ($n = 5$ bundles for each data point).

$R_{M:A}$ increases from 0.64 to 1.9 (*squares*, Fig. 2 *b*). Thus, in the absence of ATP, myosin thick filaments facilitate the formation of cross-linked actin bundles with similar mechanical behaviors over a wide range of myosin densities. Interestingly, bundles fail to form when myosin thick filaments are replaced with similar concentrations of smooth muscle heavy meromyosin, indicating the importance of thick filament architecture for bundle formation (data not shown).

Contraction occurs above a critical myosin concentration

To initiate myosin catalytic activity, Assay Buffer containing ATP is perfused into the chamber. For bundles formed with sparse myosin cross-linking ($R_{M:A} = 0.44$), the addition of 1 mM ATP results in rapid disintegration of a majority of bundles (Fig. 2, *a* and *c*, Movie S3). Concomi-

tantly, ~80% of the myosin dissociates from F-actin (see Fig. 2 *d*) and within 40 s, only F-actin bound to beads remains in the field of view (Fig. 2 *a*). Myosin does not remain bound to individual F-actin, reflecting a weak affinity of thick filaments to F-actin in the presence of ATP (30). This reduced effectiveness of myosin filament cross-links in the presence of ATP is likely the cause of bundle disintegration for bundles with $R_{M:A} < 0.44$ (see Supporting Material).

When $R_{M:A}$ is increased to 0.64, a qualitatively different behavior is observed. After perfusion of 1 mM ATP, ~40% of the myosin detaches (Fig. 2 *d*) but a majority of bundles remain intact several minutes after buffer exchange (Fig. 2, *a* and *c*, Movie S4). The amplitude of the transverse fluctuations cannot be distinguished from those before ATP addition (Fig. 2 *b*) and no change in bundle length is observed. Thus, for $R_{M:A} = 0.64$, bundles remain stable in the presence of ATP but are not contractile.

When $R_{M:A}$ is increased above 0.7, addition of 0.1–1 mM ATP induces a rapid contraction of nearly all bundles. During contraction, bundle contours rapidly change from wavy to straight (Fig. 2 a, Movie S5) and contracted bundles are taut with transverse fluctuations below our resolution limit, <0.002 μm^2 (Fig. 2 b). After becoming taut, ~60% of the bundles rupture ($n = 74$). Contracted bundles that do not rupture remain stable for at least 30 min, the duration of the experiment.

Thus, we find the myosin density within bundles is critical to the nature of bundle remodeling observed in the presence of ATP. When $R_{M:A}$ ~0.64, there is a sharp transition from ATP-induced bundle disintegration to contraction (Fig. 2 c). Because a fraction of myosin dissociates from the bundles after ATP addition, a mole ratio that accounts for this decrease, $R_{M:A}^{ATP}$, better reflects the stoichiometry in ATP and we determine that contraction dominates when $R_{M:A}^{ATP} \geq 0.5$.

Contraction occurs in tethered and untethered bundles at rates up to 400 nm/s

To quantify the contraction of bundles with a high density of myosin cross-bridges, $R_{M:A}^{ATP} = 1.4$, we measure their contour length as a function of time (*dashed lines*, Fig. 3, *a* and *c*). After perfusion of Assay Buffer containing ATP, bundle contours rapidly change from wavy to straight and decrease in length by ~5–10% within ~30 s at a maximal rate of ~100 nm/s (Fig. 3, *a* and *b*, Movie S6). When a connection to a neighboring bundle ruptures (*arrow*, Fig. 3 a), the change in boundary conditions accommodate an additional contraction of 15% at a rate of ~400 nm/s (Fig. 3, *a* and *b*). During contraction, transient bends within the bundle are often observed (65 s and 75 s, Fig. 3 a). After contraction stops, the contours of tethered bundles are straight, taut, and remain stable for longer than 100 s.

After a rupture event, bundles with a free, untethered end are formed (*asterisk*, Fig. 3, *a* and *c*). For untethered bundles, the only effects resisting contraction are the weak viscous drag of the surrounding media and any internal resistive force within the bundle. In comparison to tethered bundles, untethered bundles contract a significantly larger fraction of their original length (~25%, $n = 10$ bundles) with a higher rate of ~400 nm/s (Fig. 3 d). Thus, the boundary conditions change the extent and the rate of contraction. This implies that force sustained at the bundle endpoint impacts the extent and rate of bundle contraction.

Force-velocity relationship of reconstituted actomyosin bundles

The elastic polyacrylamide (PAA) gel on which the beads are bound provides a means to measure the tensile force generated during bundle contraction. Forces applied to a bead bound to the top surface induce PAA gel deformations that can be visualized if the gel is sufficiently compliant (31). An effective spring constant determined by the elastic properties of the PAA gel is used to calculate the force from the observed bead displacement (Fig. 4 a, Fig. S6). By reducing the shear elastic modulus of the PAA gel from 600 Pa (used in Figs. 1–3) to 54 Pa, we can visualize bead displacement. During contraction of bundles with $R_{M:A}^{ATP} = 1.4$, significant tensile forces are built (Fig. 4, *b* and *c*, Movie S7). In the first 5 s after ATP addition, the force increases to 250 pN as the contraction speed increases from 0 to 120 nm/s (Fig. 4, *c* and *d*). We speculate this may reflect a transient regime during the initiation of myosin mechanochemistry as ATP-containing buffer is perfused. After this initial force buildup, an inverse relationship between contraction speed and force is measured, with the speed decreasing as the forces build to ~600 pN (Fig. 4 d, *dashed line*); this presumably reflects the behavior of the system in saturating ATP. After contraction completes, the tensile force of 600 pN is stably maintained for minutes. The force at which bundle contraction stalls is narrowly peaked around 500 pN (Fig. 4 e) and no apparent correlation between the stall force and bundle length is observed (Fig. 4 f).
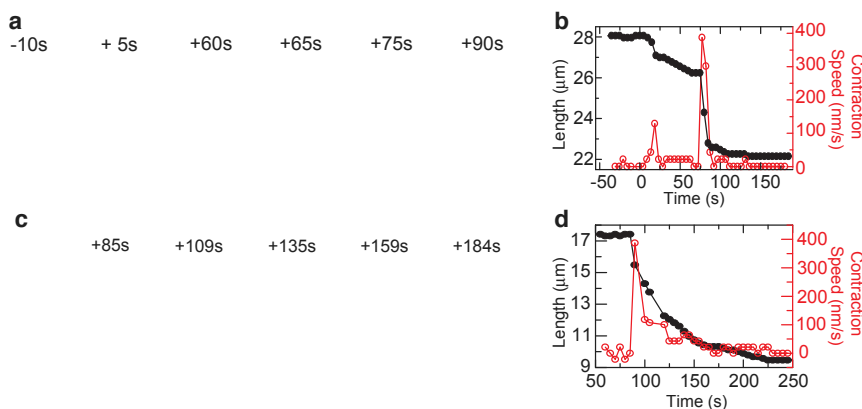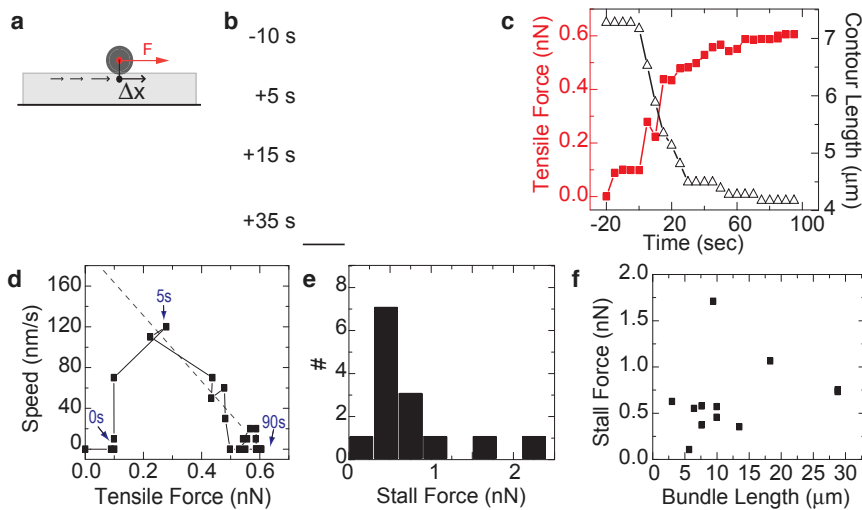

FIGURE 3 Contraction of tethered and untethered bundles. (*a*) Time-lapse series of inverted contrast, OG-myosin images in a contracting bundle with $R_{M:A}^{ATP} = 1.4$. Times are in seconds before (*negative times*) or after (*positive times*) addition of 0.1 mM ATP. Dashed line demarks changing contour of the tethered bundle of interest. A connection to a neighboring bundle breaks between 60 and 65 s (*arrow*), following which contraction of both the untethered bundle (*asterisk*) and tethered bundle (*dashed line*) resume. Scale bar is 5 μm; see Movie S6. (*b*) Contour length (*left axis, solid circles*) and contraction speed (*right axis, open circles*) of the bundle indicated by the dashed line in *a*. (*c*) Time-lapse series of inverted contrast OG-myosin images illustrating the contraction of an untethered bundle following the rupture of a taut bundle 85 s after 1mM ATP addition. Bundle shown contains $R_{M:A}^{ATP} = 1.4$. Asterisk indicates the free bundle end. Scale bar, 5 μm. (*d*) Bundle contour length (*closed circles, left axis*) and contraction speed (*right axis, open circles*) versus time for the contracting untethered bundle shown in (*c*).

a

b -10 s

+5 s

+15 s

+35 s

c

d

e

f

FIGURE 4   Tension is built during contraction of tethered bundles. (*a*) Schematic illustrating how the displacement of a bead bound to the top surface of an elastic hydrogel can be used to determine the forces applied on the bead. A force, *F*, applied to the surface-bound bead is balanced by the elastic restoring force exerted by the underlying gel, resulting in a bead displacement Δx such that $F = k_{\text{eff}} \Delta x$, where k_{eff} is an effective spring constant determined by the gel elastic properties. Further details of this measurement are discussed in Fig. S6. (*b*) Images of OG-myosin (inverted contrast) in a bundle with $R_{\text{M:A}}^{\text{ATP}} = 1.4$. The underlying gel has a shear elastic modulus of 54 Pa. Time = 0 s delineates addition of 1 mM ATP. Scale bar is 5 μm; see Movie S7. (*c*) Tensile force (*left axis, red squares*) and contour length (*right axis, open triangles*) as a function of time for the bundle shown in (*b*). (*d*) Contraction speed versus tensile force for data shown in (*b*). The dashed line approximates the force-velocity relationship observed at long times and high loads. Arrows indicate times = 0 s, 5 s, and 90 s. (*e*) Histogram of maximum tensile force, or stall force, of contractile bundles with $R_{M:A}^{ATP} = 1.4$ and contracted with buffer containing 1 mM ATP. (*f*) Stall forces calculated in (*e*) plotted as a function of initial bundle contour length.

Rate of contraction at low tension is proportional to bundle length

To measure bundle contraction rates in the absence of an external load, we examine untethered bundles contracting after a rupture event. Remarkably, the initial contraction speed strongly correlates with the initial bundle length, showing a linear dependence for both $R_{\text{M:A}}^{\text{ATP}} = 1.4$ and $R_{\text{M:A}}^{\text{ATP}} = 0.49$ (Fig. 5, *a* and *b*). Moreover, zero load contraction velocities are consistent with those obtained by extrapolating the observed inverse force-velocity relationship (*dashed line*, Fig. 4 *d*) to zero load (*open squares*, Fig. 5 *a*). The linear nature of the correlation between contraction speed and bundle length indicates a well-defined contraction speed per unit length of bundle, $\dot{\gamma} = 0.04$ s^{-1} for $R_{\text{M:A}}^{\text{ATP}} = 1.4$. When the myosin density is decreased to $R_{\text{M:A}}^{\text{ATP}} = 0.49$, $\dot{\gamma}$ decreases to 0.02 s^{-1} (Fig. 5 *b*).

To directly visualize contraction within the bundle, we examine the myosin intensity along the bundle contour (Fig. 5, *c* and *d*). Variations in myosin intensity are observed along the bundle but are <10% of the mean myosin intensity at all times during contraction (Fig. 5, *c* and *d*). During contraction, relative movements of fiduciary marks within the bundle are observed and a variety of local rearrangements ranging from highly contractile to weakly extensile are observed along the bundle length (Fig. 5 *e*). Importantly, no signature of periodic myosin intensities exist during contraction, suggesting a lack of sarcomeric organization within the bundles throughout contraction.

Bundle contraction occurs by several contractile elements connected in series

The observed length-dependent contraction velocity and length-independent stall force are consistent with bundle contraction occurring through a collection of independent contractile elements working in series. In such a model, the rate of bundle contraction is equal to the number of elements *N* multiplied by the characteristic contraction speed *v* of a single element. If contractile elements have a length *d* the number of elements in a bundle of length *L* is $N = L/d$. As a result, the length-dependent, or telescopic, bundle contraction speed is Lv/d (Fig. 6). Consequently, we expect the contraction rate per unit length observed in Fig. 5, *a* and *b* to be of the order v/d. A natural scale for the contraction speed of a single unit is to be twice that of unloaded smooth muscle myosin, ~400 nm/s (32,33). From this, we estimate d~10 μm for $R_{\text{M:A}}^{\text{ATP}} = 1.4$, approximately twice the F-actin length. As the density of myosin cross-bridges is decreased to $R_{\text{M:A}}^{\text{ATP}} = 0.49$, *d* increases to ~20 μm. Although difficult to discern from our current data, we speculate that the extent to which any given myosin filament participates as a motor or cross-linker may change over time as the load on it changes during contraction. This adaptation and malleability of contractile elements during contraction has been implicated to explain the contraction of smooth muscle cells (18).

For contractile elements arranged in series, the force generated at the bundle endpoints provides a measure of the force generated by a single element. The contractile force produced by bundles with $R_{\text{M:A}}^{\text{ATP}} = 1.4$ is strongly peaked around ~0.5 nN and the observed load-dependent contraction (Fig. 4 *d*) is consistent with the force-dependent kinetics observed in single molecules of smooth muscle myosin (10). Because the stall force of smooth muscle myosin is ~2 pN (10), this suggests that ~250 motors operate in parallel in each element, corresponding to ~3 myosin thick filaments. Because bundles consist of ~4 F-actin per cross section, we estimate that each pair of F-actin is cross-linked, on average, by 1–3 actively tensed myosin thick filaments.
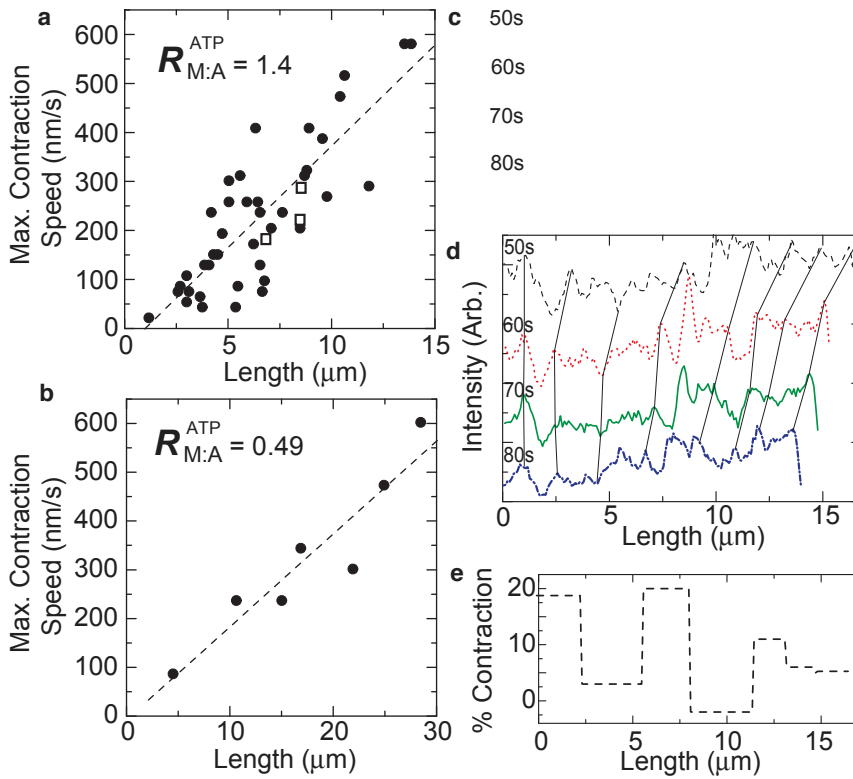
FIGURE 5 Unloaded contraction speed is proportional to bundle length. (*a*) Maximal contraction speed of untethered bundles plotted as a function of initial bundle length for $R_{M:A}^{ATP} = 1.4$ (*solid circles*). Open squares indicate zero-load velocities extrapolated from the inverse force-velocity relationship observed in Fig. 4, *d* (*dashed line*). Dashed line indicates a linear fit to the data with slope $\dot{\gamma} = 0.04$ s^{-1} ($R^2 = 0.68$). (*b*) Maximal contraction speed of untethered bundles as a function of bundle length for $R_{M:A}^{ATP} = 0.49$. Dashed lines indicate a linear fit to the data with slope $\dot{\gamma} = 0.02$ s^{-1} ($R^2 = 0.87$). (*c*) Inverted contrast images of OG-myosin during the untethered contraction following the rupture of a bundle with $R_{M:A}^{ATP} = 1.4$. Scale bar is 5 μm. (*d*) Line scans of myosin fluorescence intensity along bundle length averaged over a width of 0.5 μm for the images shown in (*c*), showing variations in myosin intensity. Solid black lines indicate guides to observe the movement of fiduciary marks. (*e*) The ratio of the change in distance between two fiduciary marks relative to their initial distance for the fiduciary marks visualized in (*d*) for times between 50 and 60 s. This measure of the percent contraction shows variations in the extent of contraction along the bundle length.

DISCUSSION

Here we have developed a versatile technique to measure the stability and force-generation in bundles consisting of F-actin and myosin thick filaments on cellular length (5–50 μm) and force (0.1–5 nN) scales. We expect this assay will be useful in determining the roles of myosin thick filament architecture, passive cross-linking proteins, and F-actin polymerization dynamics in the contraction of actomyosin bundles. We also expect this could be more generally used
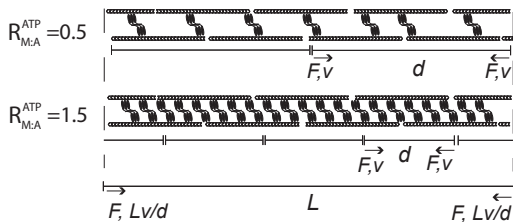

FIGURE 6 Bundle contraction operates as a series of individual contractile units Cartoons illustrating our model of how myosin densities affect the length *d* of contractile elements within the bundle. F-actin (*chevrons*) is bundled through the cross-linking of myosin thick filaments (*black*). A series of contractile elements each contracting with a velocity *v* and stall force *F* will result in the observed length-dependent rate of bundle contraction *Lv/d* and length independent stall force *F*. If the speed of the contractile elements remains unchanged for different myosin densities, then the higher rate of contraction per bundle length observed with high myosin densities (Fig. 5, *a* and *b*) can be explained by a decrease in *d*.

to study force-generation in other types of bundles formed by cytoskeletal polymers and accessory proteins.

Our data demonstrate the potential of myosin cross-bridges to variably act in both cross-linking and force generating capacities. At low ATP, the high affinity of actomyosin cross-bridges facilitate cross-linking over the entire range of myosin concentrations studied, estimated to be >3 myosin filaments per F-actin (Supporting Material). In the presence of ATP, the low duty ratio of smooth muscle myosin (34) reduces the effectiveness of actomyosin interactions. With a 4% duty ratio (34), each 360 nm long myosin thick filament containing ~200 motor domains will have an average of eight motors bound at any given time (35). The observed decrease in myosin intensity upon ATP perfusion likely reflects the detachment of myosin cross-bridges with suboptimal binding to F-actin (see Supporting Material). We find that low densities of mechanochemically active myosin filaments do not provide sufficient cross-linking to maintain stable bundles. Over a narrow range of 1–4 myosin filaments per F-actin, myosin filaments provide sufficient cross-linking of F-actin to maintain a stable bundle but do not facilitate contraction (Fig. 7). Bundle contraction only occurs at extremely high myosin filament density, more than four thick filaments per F-actin (Fig. 7). We speculate that changing the effective duty ratio of thick filaments, either by altering the duty ratio of individual motors or changing the filament size, would alter the minimum threshold of
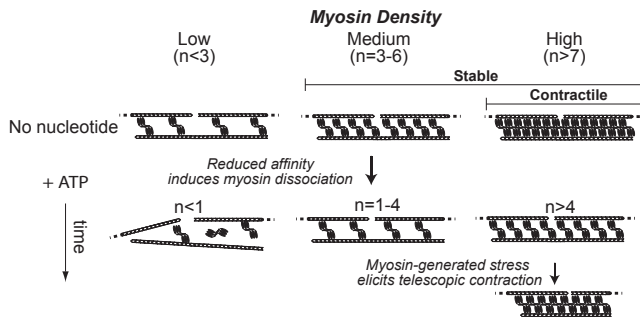
FIGURE 7 Impact of myosin filament density on bundle stability and contraction. The number *n* of myosin filaments (*black*) per F-actin (*chevrons*) is estimated from measured stoichiometries (Methods in the Supporting Material). In the absence of nucleotide, bundles are stable over a wide range of thick filament density (*top row*). ATP addition reduces the affinity of myosin cross-bridges by initiating motor mechanochemistry (*middle row*). A portion of thick filaments dissociate, leading to loss of bundle structure under low ($n < 1$) myosin densities. Intermediate myosin densities ($n = 1$–4) retain enough cross-linking within bundles to resist ATP-induced bundle disintegration, but no contraction is observed. At the highest myosin densities ($n > 4$), myosin-generated forces lead to bundle contraction (*bottom row*).

motor density required for bundle stabilization and contraction. Furthermore, in the myosin preparation used here, 50% of the regulatory light chains were phosphorylated. Preparations with 100% phosphorylation may yield different results (see Supporting Material).

Our study also shows that a high density of myosin cross-bridges is sufficient to elicit contraction and force generation in mesoscopic actomyosin bundles in the absence of other actin cross-linking or regulatory proteins. Previous in vitro experiments have concluded that passive cross-linking proteins (e.g., *α*-actinin or filamin) are required to elicit such contraction. This discrepancy can be accounted for by considering that, for previous experiments, $R_{\mathrm{M:A}} \leq 0.05$ (23,24). Here, we find that bundle contraction occurs only when $R_{\mathrm{M:A}} > 0.75$. We cannot completely exclude the existence of high affinity, dead motors serving as passive cross-linkers in our experiment. However, the limited range of $R_{\mathrm{M:A}}$ over which bundling without contractility is observed (Fig. 2 *c*) suggests that high affinity cross-links are rare (see Supporting Material). It will be interesting to explore how the nature of the observed phase diagram is altered in the presence of exogenous actin cross-linking proteins. Because the molar ratio of myosin to actin in smooth muscle cells is 0.2–0.5 (36), actin binding proteins likely play important roles in physiological regulation of contraction.

In striated myofibrils, sarcomeres are the basic contractile element and sarcomeric organization is essential for models of force transmission from the molecular to tissue length scales. However, contractile elements lacking apparent sarcomeric organization have also been proposed for smooth muscle and nonmuscle cells (9,17,19), but an understanding of the molecular or structural requirements of nonsarcomeric contraction has been lacking. Interestingly, the reconstituted bundles shown here lack myosin bands indicative of sarcomeric organization but still form contractile elements that support telescopic contraction of actomyosin bundles. Our data thus offer new, to our knowledge, perspectives on the molecular requirements and physical mechanisms of nonsarcomeric modes of contraction, such as those found in smooth muscle and nonmuscle cells (7,9).

Here, we have shown that actin filaments and mechanochemically competent myosin thick filaments self-organize into contractile elements that can transmit actomyosin forces to cellular length scales. Future work is required to determine whether these interactions can be harnessed to modify F-actin length, sort F-actin polarity, or alter myosin localization, which could result in sarcomere-like organization. We anticipate our study will serve as a starting point for more sophisticated in vitro models that will elucidate mechanisms of force transmission in the actomyosin cytoskeleton and provide insight into the design principles of adaptive biological materials.

SUPPORTING MATERIAL

REFERENCES

1. Wozniak, M. A., and C. S. Chen. 2009. Mechanotransduction in development: a growing role for contractility. *Nat. Rev. Mol. Cell Biol.* 10:34–43.

2. Vicente-Manzanares, M., X. Ma, …, A. R. Horwitz. 2009. Non-muscle myosin II takes centre stage in cell adhesion and migration. *Nat. Rev. Mol. Cell Biol.* 10:778–790.

3. Pollard, T. D. 2010. Mechanics of cytokinesis in eukaryotes. *Curr. Opin. Cell Biol.* 22:50–56.

4. Kee, A. J., P. W. Gunning, and E. C. Hardeman. 2009. Diverse roles of the actin cytoskeleton in striated muscle. *J. Muscle Res. Cell Motil.* 30:187–197.

5. Gunst, S. J., and W. Zhang. 2008. Actin cytoskeletal dynamics in smooth muscle: a new paradigm for the regulation of smooth muscle contraction. *Am. J. Physiol. Cell Physiol.* 295:C576–C587.

6. Verkhovsky, A. B., and G. G. Borisy. 1993. Non-sarcomeric mode of myosin II organization in the fibroblast lamellum. *J. Cell Biol.* 123:637–652.

7. Cramer, L. P. 1999. Organization and polarity of actin filament networks in cells: implications for the mechanism of myosin-based cell motility. *Biochem. Soc. Symp.* 65:173–205.

8. Vavylonis, D., J. Q. Wu, …, T. D. Pollard. 2008. Assembly mechanism of the contractile ring for cytokinesis by fission yeast. *Science.* 319:97–100.

9. Herrera, A. M., B. E. McParland, …, C. Y. Seow. 2005. 'Sarcomeres' of smooth muscle: functional characteristics and ultrastructural evidence. *J. Cell Sci.* 118:2381–2392.

10. Veigel, C., J. E. Molloy, …, J. Kendrick-Jones. 2003. Load-dependent kinetics of force production by smooth muscle myosin measured with optical tweezers. *Nat. Cell Biol.* 5:980–986.

11. Cooke, R. 1997. Actomyosin interaction in striated muscle. *Physiol. Rev.* 77:671–697.

12. Szent-Györgyi, A. G. 2004. The early history of the biochemistry of muscle contraction. *J. Gen. Physiol.* 123:631–641.

13. Howard, J. 2001. Mechanics of Motor Proteins and the Cytoskeleton. Sinauer Associates, Sunderland, MA.

14. Cooke, R. 2004. The sliding filament model: 1972–2004. *J. Gen. Physiol.* 123:643–656.

15. Littlefield, R., and V. M. Fowler. 1998. Defining actin filament length in striated muscle: rulers and caps or dynamic stability? *Annu. Rev. Cell Dev. Biol.* 14:487–525.

16. Huxley, H., and J. Hanson. 1954. Changes in the cross-striations of muscle during contraction and stretch and their structural interpretation. *Nature.* 173:973–976.

17. Bement, W. M., and D. G. Capco. 1991. Analysis of inducible contractile rings suggests a role for protein kinase C in embryonic cytokinesis and wound healing. *Cell Motil. Cytoskeleton.* 20:145–157.

18. Kuo, K. H., A. M. Herrera, …, C. Y. Seow. 2003. Structure-function correlation in airway smooth muscle adapted to different lengths. *Am. J. Physiol. Cell Physiol.* 285:C384–C390.

19. Carvalho, A., A. Desai, and K. Oegema. 2009. Structural memory in the contractile ring makes the duration of cytokinesis independent of cell size. *Cell.* 137:926–937.

20. Spicer, S. S. 1951. Gel formation caused by adenosine triphosphate in actomyosin solutions. *J. Biol. Chem.* 190:257–267.

21. Crooks, R., and R. Cooke. 1977. Tension generation by threads of contractile proteins. *J. Gen. Physiol.* 69:37–55.

22. Stendahl, O. I., and T. P. Stossel. 1980. Actin-binding protein amplifies actomyosin contraction, and gelsolin confers calcium control on the direction of contraction. *Biochem. Biophys. Res. Commun.* 92:675–681.

23. Janson, L. W., J. Kolega, and D. L. Taylor. 1991. Modulation of contraction by gelation/solation in a reconstituted motile model. *J. Cell Biol.* 114:1005–1015.

24. Bendix, P. M., G. H. Koenderink, …, D. A. Weitz. 2008. A quantitative analysis of contractility in active cytoskeletal protein networks. *Biophys. J.* 94:3126–3136.

25. Koenderink, G. H., Z. Dogic, …, D. A. Weitz. 2009. An active biopolymer network controlled by molecular motors. *Proc. Natl. Acad. Sci. USA.* 106:15192–15197.

26. Mizuno, D., C. Tardin, …, F. C. Mackintosh. 2007. Nonequilibrium mechanics of active cytoskeletal networks. *Science.* 315:370–373.

27. Altringham, J. D., P. H. Yancey, and I. A. Johnston. 1980. Limitations in the use of actomyosin threads as model contractile systems. *Nature.* 287:338–340.

28. Sellers, J. R. 1985. Mechanism of the phosphorylation-dependent regulation of smooth muscle heavy meromyosin. *J. Biol. Chem.* 260:15815–15819.

29. Peterson, L. J., Z. Rajfur, …, K. Burridge. 2004. Simultaneous stretching and contraction of stress fibers in vivo. *Mol. Biol. Cell.* 15:3497–3508.

30. Lymn, R. W., and E. W. Taylor. 1971. Mechanism of adenosine triphosphate hydrolysis by actomyosin. *Biochemistry.* 10:4617–4624.

31. Sabass, B., M. L. Gardel, …, U. S. Schwarz. 2008. High resolution traction force microscopy based on experimental and computational advances. *Biophys. J.* 94:207–220.

32. Sellers, J. R., J. A. Spudich, and M. P. Sheetz. 1985. Light chain phosphorylation regulates the movement of smooth muscle myosin on actin filaments. *J. Cell Biol.* 101:1897–1902.

33. Warshaw, D. M., J. M. Desrosiers, …, K. M. Trybus. 1990. Smooth muscle myosin cross-bridge interactions modulate actin filament sliding velocity in vitro. *J. Cell Biol.* 111:453–463.

34. Rosenfeld, S. S., J. Xing, …, H. L. Sweeney. 2003. Myosin IIb is unconventionally conventional. *J. Biol. Chem.* 278:27449–27455.

35. Tonino, P., M. Simon, and R. Craig. 2002. Mass determination of native smooth muscle myosin filaments by scanning transmission electron microscopy. *J. Mol. Biol.* 318:999–1007.

36. Gabella, G. 1984. Structural apparatus for force transmission in smooth muscles. *Physiol. Rev.* 64:455–477.

Supplementary Information,

Todd Thoresen, Martin Lenz and Margaret L. Gardel

a.

STD   Myosin   Actin

kDa

200

116
97

66

45

b.

i   ii   iii

RLC
RLC-P

ELC

i - Myosin
ii - Myosin w/ PPP1
iii - Myosin w/ MLCK

c.

[Myosin] (μM)
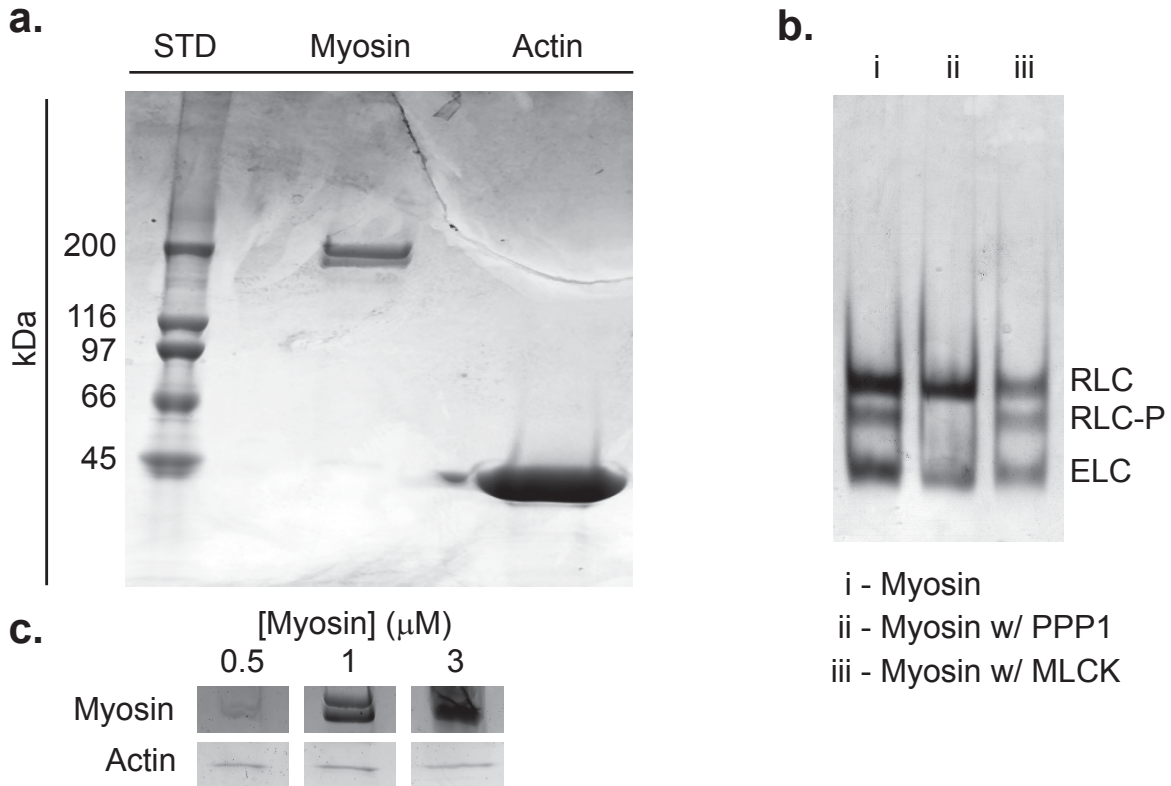
0.5   1   3

Myosin

Actin

Figure S1: **Characterization of Proteins within Bundles.** (a) SDS-PAGE of smooth muscle myosin and actin used in these experiments. A molecular weight standard (STD) is run simultaneously; corresponding molecular weights are shown. Migration of 19 kDa proteins corresponds to bottom of gel. (b) Charge gel electrophoresis (Trybus KM., 2000) was used to separate the non-phosphorylated (RLC) from the phosphorylated (RLC-P) regulatory light chains in order to quantify the extent of phosphorylation of myosin samples. The essential light chain (ELC) is also shown. (i) is natively phosporylated myosin, (ii) is myosin subject to Protein Phosphatase 1 (PPP1), (iii) is myosin phosphory-lated with myosin light chain kinase (MLCK). Through densitometry, the % phosphoryla-tion is 25%, 6%, and 46% for lanes (i), (ii) and (iii), respectively. (c) Myosin heavy chain and actin bands from SDS-PAGE analysis for bundles formed with different myosin con-centrations, as shown.
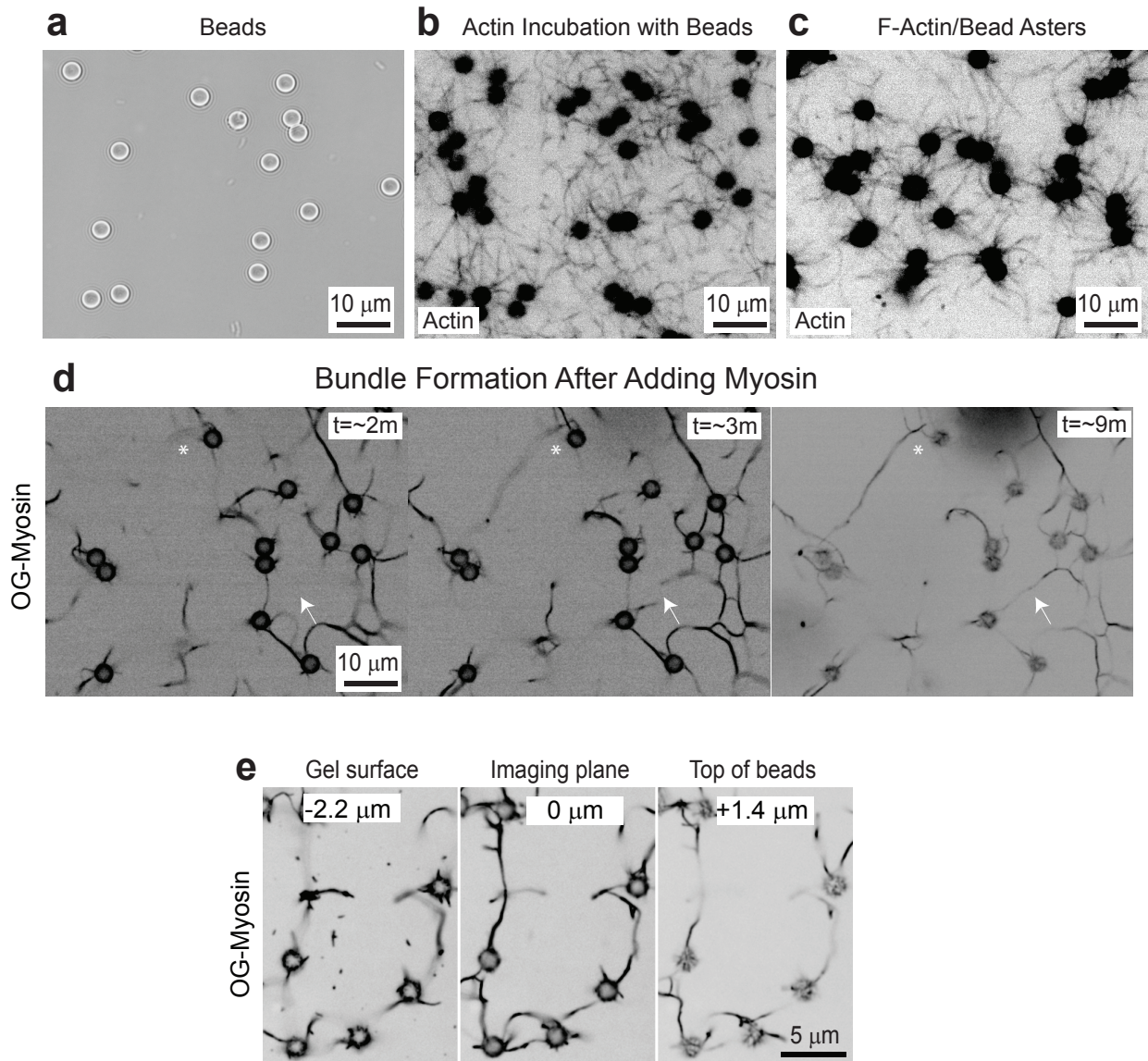
Figure S2: Templated Assembly of Actomyosin Bundles. (a) Neutravidin-coated beads visualized with bright field microscopy. (b) Image of Alexa 568 phalloidin-stabilized F-actin containing 10% biotinylated actin during bead incubation. (c) Image after removal of the majority of unbound actin through buffer wash. (d) Images of Oregon Green labeled myosin (OG-Myosin) at several different times after OG-myosin addition. The first image is obtained after perfusion is finished (~2 min after OG-myosin is introduced). Some bundles form from cross-linking of existing bundles (arrow), while others form in solution then bind to asters (asterisk). (e) Images of OG-Myosin at the PAA gel surface (-2.2 μm), at the plane of imaging (0 μm) and near the top of the 3 micron beads (+1.4 μm). All fluorescence images are inverted contrast.

a.

Surface Adsorbed F-actin

b.

Distribution of F-Actin Lengths

c.

Max. Int. of F-actin Cross-section

d.

EM of Myosin
Thick Filaments
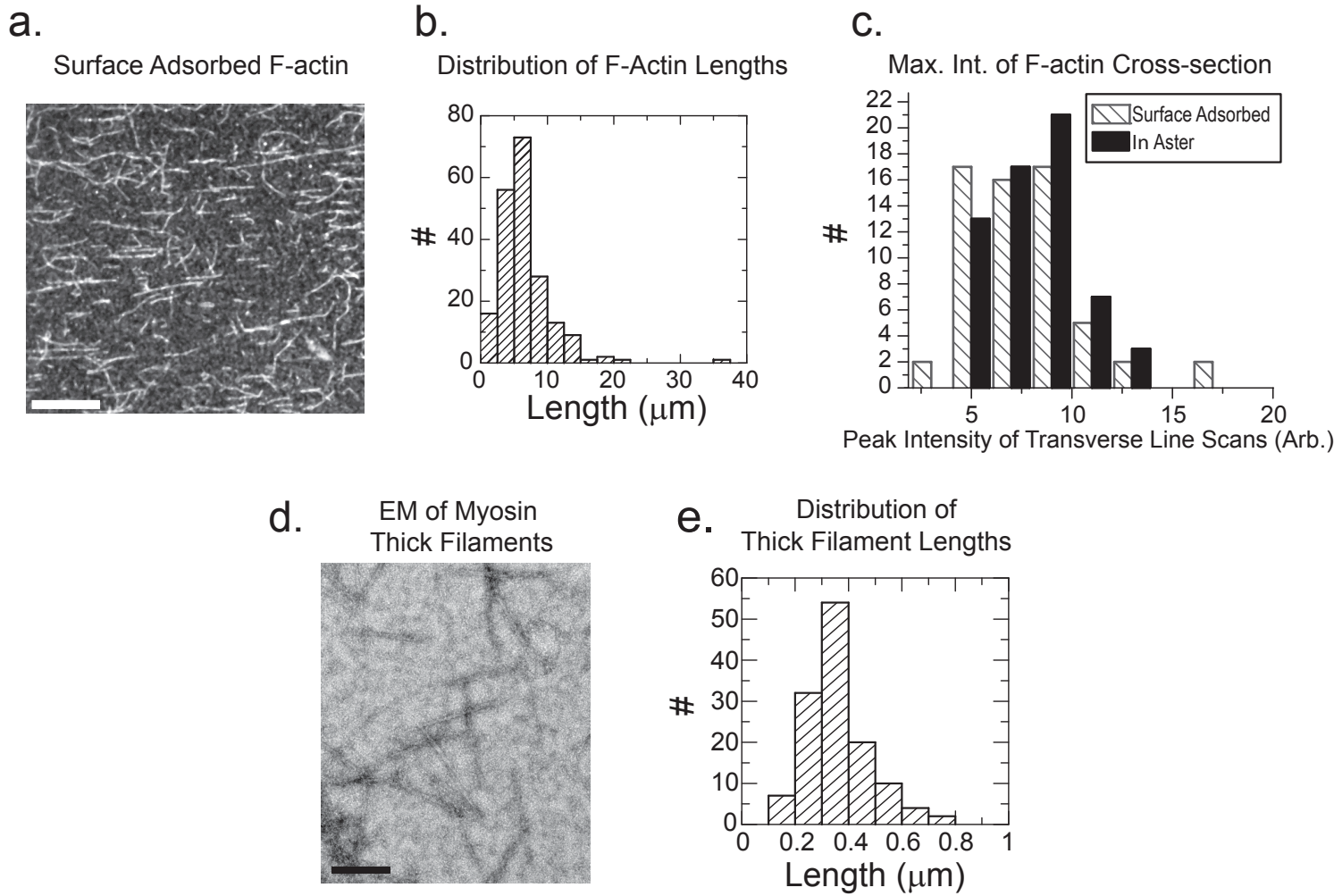

e.

Distribution of
Thick Filament Lengths

Figure S3: Characterization of F-actin lengths and total F-actin contained within Asters and Bundles. (a) Image of F-actin, visualized with Alexa 568 phalloidin, bound to a glass coverslip. Scale bar = 10 μm. (b) Histogram of F-actin lengths. Lengths are 6.5 ± 4.0 μm (mean ± s.d., n = 200). (c) Background-subtracted peak intensity of transverse line scans across F-actin adsorbed on the surface (n = 61) and in F-actin asters (n = 61). (d) Electron micrograph image of 1 μM smooth muscle myosin thick filaments. Scale bar = 0.2 μm. (e) Histogram of myosin thick filament lengths. Lengths are 0.36 ± 0.1 μm (mean ± s.d., n = 130).
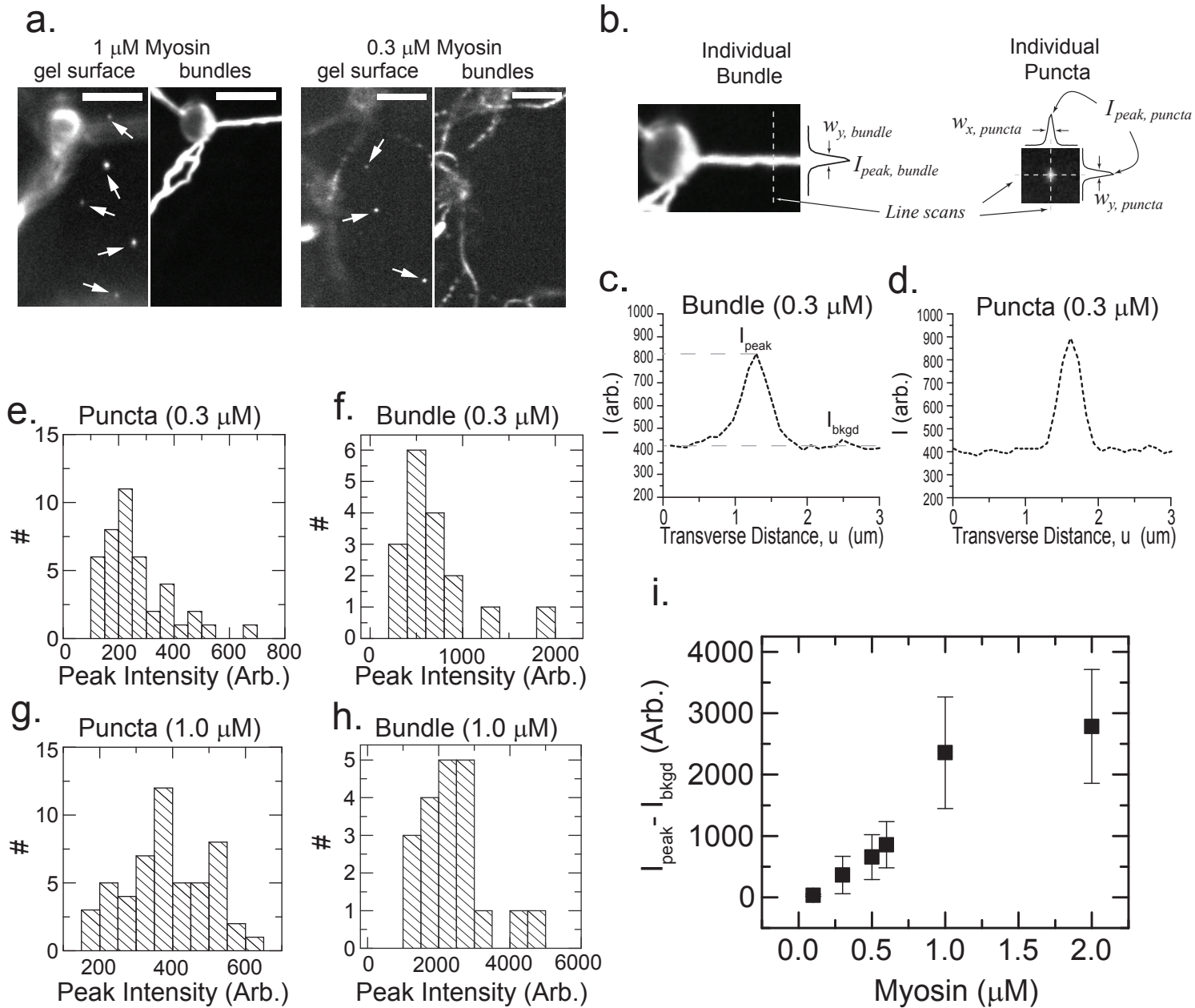
Figure S4: Quantification of Myosin Thick Filament and Bundle Intensities. (a) Images of OG-myosin in the focal plane of the gel surface or bundles prepared with either 1.0 or 0.3 μM myosin. At the gel surface, diffraction-limited puncta are presumed individual myosin filaments (arrows), and out of focus features are bundles. (b) Schematic indicating how line scans accross actomyosin bundles and myosin puncta were taken, with peak intensities (I_{peak}) and full width half max indicated. (c) Representative transverse line scan accross a bundle shown in (a, 0.3 μM myosin, right). (d) Line scan across a myosin puncta in (a) at gel surface (0.3 μM myosin, left). (e) Histogram of background-subtracted peak intensities of similar puncta found in (a, 0.3 μM myosin, left). Mean intensity is 259 ± 118 (s.d., n = 41). (f) Histogram of background-subtracted peak intensities of bundles represented in (a, 0.3 μM myosin, right). Mean intensity is 656 ± 366 (s.d., n = 17). (g) Histogram of background-subtracted peak intensities of puncta represented in (a, 1.0 μM myosin, left). Mean intensity is 381 ± 117 (s.d., n = 52). (h) Histogram of background-subtracted peak intensities of bundles represented in (a, 1.0 μM myosin, right). Mean intensity is 2733 ± 1092 (s.d., n = 20). (i) Mean peak intensities of transverse line scans accross bundles as a function of myosin concentration used. Error bars indicate s.d., n = 20 bundles for each data point.
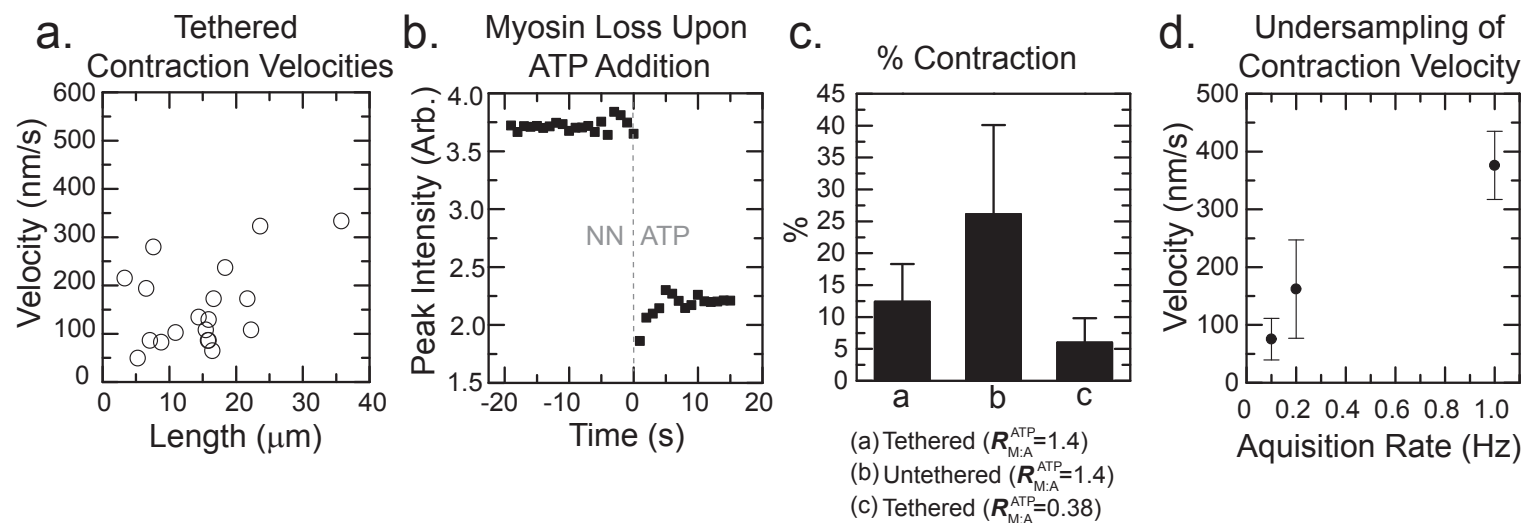
a. Tethered Contraction Velocities

b. Myosin Loss Upon ATP Addition

NN | ATP

c. % Contraction

(a) Tethered ($R_{M:A}^{ATP}$=1.4)
(b) Untethered ($R_{M:A}^{ATP}$=1.4)
(c) Tethered ($R_{M:A}^{ATP}$=0.38)

d. Undersampling of Contraction Velocity

Figure S5: Contractile Behavior. (a) Maximal velocity of contraction observed for tethered bundles as a function of initial bundle length for bundles formed with $R_{M:A}^{ATP}$ = 1.4. (b) Background-subtracted myosin peak intensity in a bundle ($R_{M:A}^{ATP}$= 1.4) over time. 1 mM ATP is added at 0 s. (c) The amount of contraction, measured as the change in contour length divided by the initial contour length, for untethered and tethered bundles with $R_{M:A}^{ATP}$= 1.4, (n = 40 and 34 bundles, respectively) and for teth-ered contraction for bundles with $R_{M:A}^{ATP}$= 0.38 (n = 20 bundles). (d) Measured contraction speed as a function of aquisition rate. We estimate undersampling has a ~2-fold effect on reported velocities, as most of the data in this study was acquired at a frame rate of 0.2 frames per second. Error bars are s.d., sample sizes of n = 6 (1 Hz), n = 8 (0.2 Hz) and n = 15 (0.1 Hz) bundles.
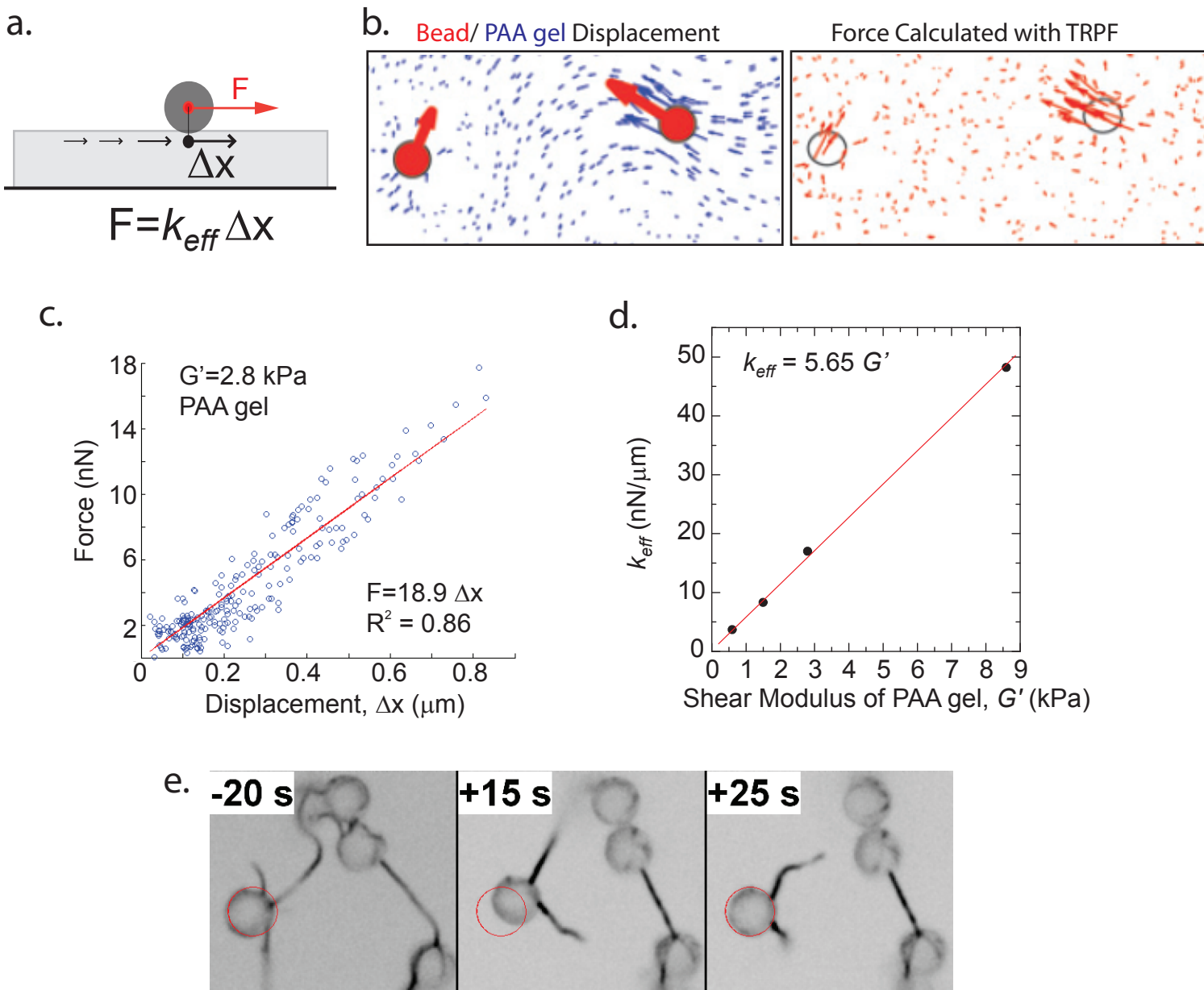
Figure S6: Calculation of Tensile Force. (a) Schematic illustrating the gel displacements resulting from a shear force exerted at a single point on the top surface of the gel. (b) Simulation data from Fig 4 of (Sabass *et al.*, *Biophys. J.*, 2008) showing the relationship between the bead displacement, the displacement field of the underlying gel and calculation of traction forces using Traction Reconstruction with Point Forces (TRPF) (c) A linear dependence between force, F , and bead displacement, Δx, for traction force data obtained with a 2.8 kPa PAA gel (Stricker *et al.*, *J. Phys. Condens. Matter*, 2010). The slope of this line is the effective spring constant k_{eff} = 18.9 nN/μm. (d) The measured k_{eff} as a function of the shear elastic modulus, G', of the PAA gel. Here we work with 54 Pa gels and determine a k_{eff} = 0.38 nN/μm. (e) Montage of OG-myosin images (inverted contrast) of bundles with $R_{M:A}^{ATP}$ = 1.4 tethered to beads placed on the surface of a polyacrylamide (PAA) gel with a G' = 54 Pa. Bead position is determined prior to 1 mM ATP addition (red circle). After ATP is added at time = 0 s, contraction occurs and displaces beads in the direction of the bundle. After bundle rupture occurs at 20 s, the bead returns to its original position, indicating an elastic restoring force between the bead and the PAA gel.

MATERIALS AND METHODS

Buffers
Myosin Storage Buffer: 50 mM HEPES, pH 7.6, 0.5 M KCl, 1 mM DTT
Myosin Spin-Down Buffer: 20 mM MOPS, pH 7.4, 500 mM KCL, 4 mM $MgCl_2$, 0.1 mM EGTA, 500 µM ATP
G-actin Buffer (G-Buffer): 2 mM Tris-HCl, pH 8.0, 0.2 mM ATP, 0.2 mM $CaCl_2$ 0.2 mM DTT, 0.005% NaN_3
F-actin Buffer (F-Buffer): 10 mM imidazole, pH 7.0, 1 mM $MgCl_2$, 50 mM KCl, 2 mM EGTA
Wash Buffer : 20 mM MOPS, pH 7.4, 50 mM KCL, 4 mM $MgCl_2$, 0.1 mM EGTA
Assay Buffer : 20 mM MOPS, pH 7.4, 100 mM KCL, 4 mM $MgCl_2$, 0.1 mM EGTA, 0.7% methylcellulose, 0.25 mg/ml glucose, 0.25% β-ME, 0.25 mg/ml glucose oxidase, 35 µg/mL catalase
Contraction is initiated by perfusion of Assay Buffer containing 0.1-1 mM ATP, a sufficiently high concentration for saturating kinetics of smooth muscle myosin (1, 2).

Protein Preparations
Myosin Purification: All purification takes place at 4°C. Native smooth muscle myosin is purified from fresh chicken gizzards essentially as described previously, except myosin is actively phosphorylated using myosin light chain kinase (MLCK) prior to storage (3) in order to minimize heterogeneity due to phosphorylation-dependent configurations (4). Fluorescent labeling of myosin is performed using Oregon Green (OG) 488 maleimide dye (Molecular Probes, Invitrogen) as described previously (5). The labeling ratio is 3.6 dye per myosin dimer. Myosin is concentrated using Amicon Ultra-15 centrifugal filters (Millipore, 100 kDa cutoff) to 18 mg/ml in Myosin Storage Buffer, then drop frozen in liquid nitrogen for long term storage. Smooth muscle heavy meromyosin (HMM) and calmodulin are given by Dr. Melanie Norstrom (Rock lab, University of Chicago). MLCK is a generous gift from Dr. Primal de Lanerolle (University of Illinois, Chicago). Reported mole ratios and molar concentrations for myosin refer to myosin heavy chain and its two light chains (M_w=237 kDa).

Myosin Thick Filament Formation: Snap frozen aliquots of OG-labeled and phosphorylated myosin are rapidly thawed. To separate the fraction of myosin dimers that bind with high affinity to F-actin in saturating ATP (and presumed to be enzymatically dead) from the fraction that binds with weak affinity to F-actin in saturating ATP (and presumed to be enzymatically active), myosin dimers are mixed with phalloidin-stabilized F-actin at a 1:5 myosin:actin molar ratio in Spin-down Buffer and centrifuged for 30 minutes at 100,000g. The supernatant contains myosin with low affinity to F-actin, whereas the high affinity binding fraction co-sediments with the F-

actin pellet. Myosin protein concentrations are determined spectroscopically using an extinction coefficient at 280 nm of 0.56 ml mg^{-1} cm^{-1} compared to a myosin-free sample that includes nucleotide. Polymerization of myosin thick filaments are formed by diluting myosin in Assay buffer, thus changing the salt conditions from 500 mM to 120 mM KCl and waiting 10 minutes at room temperature.

Actin Purification: Actin is purified from rabbit skeletal acetone powder and stored in G-buffer at -80 C. (G-actin is generously supplied by Dr. David Kovar (University of Chicago)). Biotinylated actin is prepared using EZ-Link NHS-PEO$_4$ biotinylation kit (Thermo Scientific).

Actin Filament Preparation: Prior to polymerization with F-buffer, biotinylated actin is mixed with unlabeled actin in a 1:10 stoichiometry. Alexa 568-phalloidin (Molecular Probes) is added in a 2:1 mole ratio (phalloidin:actin) to both stabilize F-actin and for visualization in fluorescence imaging.

Bead Preparation

3 micron diameter polystyrene carboxylate beads (Polysciences) are biotinylated using EZ-Link NHS-PEO$_4$ biotinylation kit (Thermo Scientific) and subsequently coated with 5 mg/ml neutravidin (Thermo Scientific). The beads are repeatedly spun down (15,000g, 5 min) and resuspended 10 times in PBS. The beads are then briefly sonicated and stored at 4°C undergoing constant rotation.

Coverslip Preparation

A polyacrylamide gel is polymerized on the coverslip surfaces (22 mm diameter #1½, EMS) as described previously (6, 7). Acrylamide and bis-acrylamide concentrations are chosen to form gels with a shear elastic modulus of 600 Pa (5% acrylamide/0.075% bis) or 54 Pa (3% acrylamide/0.04% bis), as measured with a stress-controlled rheometer. 1 mg/ml biotinylated BSA, formed by reacting BSA (Sigma) with NHS-Biotin (Thermo Scientific) is covalently attached to the gel surface using sulfo-SANPAH (Thermo Scientific) using previously described techniques (6, 7). Cover slips are washed in PBS and stored at 4°C and used within 2 weeks. All data shown was obtained on a 600 Pa gel surface except that in Fig. 4, which was obtained on a 54 Pa gel surface.

Assembly of F-actin Asters

A sequential series of steps is used to template the assembly of bundles existing predominately within a single confocal imaging plane and tethered at their ends to facilitate force measurement. First, a 10-20 μm thick polyacrylamide (PAA) gel is formed on a coverslip and biotinylated-bovine serum albumin (BSA) is covalently attached to the top surface as described above. This biotinylated BSA-PAA substrate

provides a surface largely inert to non-specific myosin or actin binding and facilitates traction force microscopy (6). The substrate is then loaded into a flow chamber customized for imaging with high numerical aperture objectives and small (~30 μL) exchange volumes. After assembling the perfusion chamber, water is perfused through the sample to maintain hydration of PAA gel prior to starting the experiment.

A dilute suspension of 3 μm diameter neutravidin beads in Wash buffer is perfused into the flow chamber and incubated for ~10 minutes to allow for the beads to sediment and bind to the biotinylated-BSA surface (Fig. S2a). Unbound beads are then removed by further perfusion of Wash Buffer. We aim for an average distance between beads > 10 μm but observe variations between experiments; the conclusions presented are not affected by the bead density. Alexa 568 phalloidin-stabilized F-actin containing 10% biotinylated G-actin is gently sheared to a length of 6 μm (Fig. S3a+b), diluted to 1 μM in Assay Buffer and perfused into the chamber. Over the course of 30 minutes, F-actin binds to the avidin beads. A majority of free, unbound F-actin is removed by perfusion of two chamber volumes of Assay Buffer (Fig. S2b+c). The remaining bead-bound F-actin provides sites to template the assembly of actomyosin bundles (Fig. 2a-b, Fig. S3c, Movie S1). Since biotinylated G-actin is randomly incorporated into F-actin during polymerization, free F-actin ends emanating from beads (asterisks, Fig. 1b) are likely of random polarity. The formation of F-actin asters is not sensitive to small changes in wash steps, but is extremely sensitive to air bubbles within the flow chamber.

Microscopy

Light Microscopy: A customized flow chamber was used from Chamlide Live Cell Imaging. Fluorescence imaging is performed using a Ti-E microscope body (Nikon) fitted with a CSU-X spinning disc confocal head (Yokogawa), a HQ2 CoolSnap CCD camera (Roper Scientific) and a 60x 1.2NA water immersion objective lens (Nikon). The instrument is controlled with Metamorph software (MDS Analytical Technologies). All images shown are inverted contrast with low pass filtering. In Fig. 1b and in Movie S1, low fluorescence intensities of individual F-actin are enhanced by altering the gamma of the image.

Electron Microscopy: Electron microscopy was performed by incubating a carbon-coated copper grid with 100 nM of myosin thick filaments for 1 minute at room temperature. The grid was subsequently washed with 3 drops (~10 μL) of deionized water. One drop of 1% uranyl acetate was applied and washed with 3 more drops of deionized water. The sample was dried by wicking with filter paper, and then inserted into a FEI Tecnai F30 electron microscope for visualization.

Image Analysis

Measurement of $R_{M:A}$ and number of myosin filaments per F-actin

Quantitative fluorescence imaging to determine bundle composition is obtained by analyzing F-actin or myosin images acquired using the same laser power and acquisition settings and corrected for photobleaching. To determine the average fluorescence signal in the bundle, the peak intensity of a transverse line scan across an F-actin or actomyosin bundle averaged over a 1 μm length of the bundle is determined, corrected for photobleaching and background subtracted.

To quantify the actin and myosin within bundles, the intensity of actin and myosin in the bundle were compared to intensity of individual F-actin and myosin puncta (presumed to be thick filaments) bound to a glass coverslip or gel surface. Transverse line scans across individual F-actin, myosin puncta or bundles all yielded a Gaussian-like profile characterized by a peak intensity, I_{peak}, and a full-width half max, w (e.g. Fig. 1d). For all features, $w \sim 300$ nm, indicating a width at or near the diffraction limit.

The number of F-actin per bundle cross-section is determined by comparing the background-subtracted peak intensity of transverse line scans across Alexa 568-phalloidin stabilized actin filaments on the surface of a glass coverslip, I_F, to that across a bundle, I_B. Since the widths of the filament and bundle are similar, the total number of F-actin per bundle cross-section is $n^x_{F-actin} = I_B/I_F$. Images of F-actin and bundles are acquired on the same day using the same stock Alexa 568 phalloidin - actin to ensure identical labeling density.

The total number of actin monomers contained in a bundle of length L is determined by:
$$N_{G-actin} = n^x_{F-actin} \cdot \rho_{F-actin} \cdot L$$
where $\rho_{F-actin}$=360 G-actin/μm is the number of G-actin per micron of actin filament (8)

We presume that puncta of OG-myosin observed sparsely on the gel surface to be individual myosin thick filaments. We find this a reasonable assumption given previous experience with imaging individual myosin filaments. Furthermore, puncta intensities observed in several different conditions are similar (Fig. S4a, e+f) and the mean myosin filament length, $\ell_{myo.fil} = 360 \, nm$, is consistent with the diffraction-limited feature observed by light microscopy.

The total number of myosin filaments for a bundle of length L is determined by the ratio of the total myosin intensity in the bundle, $I_{peak,bundle} \cdot w \cdot L$, to the total myosin intensity in an individual puncta, $\left(I_{peak,puncta} \cdot w^2 \right)$:
$$N_{myo.fil} = \left(I_{peak,bundle} \cdot L \right) / \left(I_{peak,puncta} \cdot w \right)$$

The number of myosin heavy chains in a length of bundle is then determined by:

$$N_{myosin\ heavy\ chains} = N_{myo.puncta} \cdot \rho_{myo.fil} \cdot \ell_{myo.fil}$$

where $\rho_{myo.fil}$ = 0.5 heavy chains/µm is the linear density of myosin heads in a smooth muscle myosin thick filament (9) Finally, the mole ratio of myosin heavy chains to actin monomers is determined by:

$$R_{M:A} = \frac{N_{myosin\ heavy\ chains}}{N_{G-actin}}$$

The mole ratios we determined from quantitative imaging were consistent with those obtained from densitometry of similar bundles (Fig. 1f).

To quantify the number of myosin thick filaments per actin filament in our experiment, we first consider the total number of F-actin in a bundle of length L

$$N_{F-actin} = n_{F-actin}^{x} \cdot L/\ell_{F-actin}$$

where $\ell_{F-actin}$ = 6 µm is the mean length of F-actin in our experiment (Fig. S3b). The number of myosin thick filaments per F-actin is then given by:

$$n = \frac{N_{myo.fil}}{N_{F-actin}}$$

Quantification of Bundle Fluctuation: Transverse line scans are taken across bundle midpoints and the location of the bundle (identified by the peak intensity) along this line scan is determined for 10-20 frames, reflecting 50-100 seconds. The variance of this position is used to calculate the magnitude of transverse fluctuations.

Quantification of Contraction: Bundles are manually identified and bundle length is measured by using a multi-segmented line tool within Metamorph (MDS); error in identification of bundle length occur both from user bias (~5 pixels, (0.5 µm)) and the confocal depth of field (~0.5 µm). All our measurements are taken at identical frequencies 0.2 Hz to minimize undersampling effects (Fig. S5).

Force Measurements: Using traction force reconstruction with point forces to calculate force from a displacement field on the top surface of a PAA gel (6), the force is related to the local gel displacement by an effective spring constant, k_{eff} (Fig. S6a-c). As expected, k_{eff} varies linearly with the PAA gel stiffness (Fig. S6d). Assuming deformation of the polystyrene bead ($G'\sim10^{9}$ Pa) is negligible compared to that of the soft PAA gel (G'= 54 -600 Pa), the bead displacement is then multiplied by the k_{eff} to measure the force produced during contraction (Fig 4a). For a 600 Pa gel used in Figs. 1-3, k_{eff} ~3.39 nN/µm and a force of 0.7 nN is required for bead displacements of 200 nm, near our ability to resolve bead displacement. On these stiff gels, we rarely resolve bead motion. When G' is decreased to 54 Pa, k_{eff} = 0.3 nN/µm. On these substrates (used in Fig. 4), we always resolve bead displacements for bundles formed with saturating density of myosin ($R_{M:A}^{ATP}$=1.4).

Densitometry: F-actin and OG-myosin filaments were prepared as described above. A 100 nM suspension of phalloidin-stabilized F-actin was mixed with was mixed with 0.1, 0.5, 1 and 3 µM OG-myosin filaments to form a dilute suspension of actomyosin bundles qualitatively similar to those obtained in by templated bundle assembly, as confirmed with fluorescence microscopy. Bundles were isolated from individual F-actin and myosin by low speed centrifugation (5000 g, 10 min) at room temperature and analyzed using SDS-PAGE. The gel image was analyzed using ImageJ to quantify the background-subtracted intensities of bands corresponding to myosin heavy chain and actin. The mole ratio of myosin heavy chain to actin in bundles was determined

Supplemental Text

Contribution of unphosphorylated smooth muscle myosin

The extent of myosin light chain phosphorylation is ~50% for the smooth muscle myosin preparation (Fig S1b). In principle, this is consistent with an entire population of active species comprised of a singly-phosphorylated dimer (10, 11). However, since we do not know the distribution of singly or doubly phosphorylated dimers, we cannot dismiss the existence of a population of unphosphorylated myosin dimers used in our experiments. Thus, our results may be altered if the myosin preparation was 100% phosphorylated.

In the presence of ATP, unphosphorylated myosin undergoes a conformational change (referred to as 10S) whereby the coiled-coil tail domain of an unphosphorylated myosin dimer interacts with a motor domain. The 10S conformation of smooth muscle has been characterized as catalytically inactive and unsuitable for incorporation within thick filaments (12-14).

The loss of myosin intensity within bundles upon ATP addition (Fig. 2b) is consistent with some population adopting this 10S conformation. However, we do not think that this effect is dominant. In particular, the fractional loss of myosin intensity shows a dependence to $R_{M:A}$ (Fig. 2b), whereas the fraction of unphosphorylated species in our samples remains constant.

Rather, we suspect that detachment of myosin thick filaments with sub-optimal binding geometries (e.g. bound at an angle, bound to only one F-actin) that occurs because of the low affinity of mechanochemically active myosin is the dominant effect. When bundles disintegrate, the reduced local density of F-actin would promote detachment conditions, consistent with the higher fraction of detached myosin.

Presence and Effect of Inactive Myosin

We have several lines of evidence to indicate that inactive, or non-cycling, myosin acting as a passive, static actin cross-linker does not play a dominant role in the behaviors observed here.

First, a removal of the fraction of myosin heads that stay bound with high affinity to F-actin in high ATP conditions prior to myosin filament formation is a crucial part of our experiment (See Methods, Preparation of Myosin filaments). If this step is not executed, a similar network of actomyosin bundles is observed, but, upon addition of 1 mM ATP, no contraction is observed.

Second, we observe ATP-dependent dissociation of a fraction of myosin for bundles that contract. In these cases, approximately 30% of the myosin dissociates from the bundle after perfusing in ATP. At lower concentrations of myosin, when bundles disintegrate, 95% of the myosin dissociate from individual F-actin, indicating that myosin thick filaments are not bound with high affinity to individual F-actin. If a significant fraction of inactive heads existed, we expect non-cycling myosin to remain irreversibly bound to individual F-actin filaments.

Consistent with these observations, mixtures of our purified thick filaments with F-actin in dilute, three-dimensional networks show behaviors as reported previously (15, 16). Indeed, no macroscopic contraction is observed with solutions of F-actin and myosin thick filaments (data not shown). Moreover, visualization of myosin mobility with the network indicates the myosin thick filaments are only weakly associated with the F-actin solution, spending most of the time freely diffusing and associating with the F-actin for no more than 30 sec at a time.

If myosin contains a fraction of enzymatically dead motors, ATP-dependent remodeling of actomyosin bundles is largely abrogated (data not shown).

Role of Myosin Thick Filament Architecture

The thick filaments of smooth muscle myosin utilized here are a side polar geometry, consistent with previous reports (17) and evidenced by both the presence of tapered ends on filaments and the lack of a visible central bare zone in electron micrographs (Figure S3). The use of heavy meromyosin smooth muscle myosin, which does not assemble into thick filaments, instead of full length smooth myosin, did not induce bundle formation (data not shown), indicating that thick filaments of myosin play a significant role in formation of actomyosin bundles.

Repeating the experiments with full length skeletal muscle myosin, which assemble into bipolar thick filaments, yielded bundles that contracted upon addition of ATP, although qualitative differences were observed both in the types of bundles formed and the rates and extent of contraction and will be discussed in a future manuscript. Thus, the thick filament geometry is not essential for mediating contractile behavior.

1.   Warshaw, D. M., J. M. Desrosiers, S. S. Work, and K. M. Trybus. 1990. Smooth muscle myosin cross-bridge interactions modulate actin filament sliding velocity *in vitro*. J. Cell Biol. 111:453-463.
2.   Onishi, H., S. V. Mikhailenko, and M. F. Morales. 2006. Toward understanding actin activation of myosin ATPase: the role of myosin surface loops. Proc Natl Acad Sci U S A 103:6136-6141.
3.   Sellers, J. R., M. D. Pato, and R. S. Adelstein. 1981. Reversible phosphorylation of smooth muscle myosin, heavy meromyosin, and platelet myosin. J. Biol. Chem. 256:13137-13142.
4.   Lowey, S., and K. M. Trybus. Common Structural Motifs for the Regulation of Divergent Class II Myosins. Journal of Biological Chemistry 285:16403-16407.
5.   Verkhovsky, A. B., and G. G. Borisy. 1993. Non-sarcomeric mode of myosin II organization in the fibroblast lamellum. J Cell Biol 123:637-652.
6.   Sabass, B., M. L. Gardel, C. M. Waterman, and U. S. Schwarz. 2008. High resolution traction force microscopy based on experimental and computational advances. Biophys J 94:207-220.

7.   Aratyn-Schaus, Y., P. W. Oakes, J. Stricker, S. P. Winter, and M. L. Gardel. 2010. Preparation of complaint matrices for quantifying cellular contraction. J Vis Exp.

8.   De La Cruz, E. M., A. Mandinova, M. O. Steinmetz, D. Stoffler, U. Aebi, and T. D. Pollard. 2000. Polymerization and structure of nucleotide-free actin filaments. J Mol Biol 295:517-526.

9.   Tonino, P., M. Simon, and R. Craig. 2002. Mass Determination of Native Smooth Muscle Myosin Filaments by Scanning Transmission Electron Microscopy. Journal of Molecular Biology 318:999-1007.

10.   Walcott, S., P. M. Fagnant, K. M. Trybus, and D. M. Warshaw. 2009. Smooth muscle heavy meromyosin phosphorylated on one of its two heads supports force and motion. J Biol Chem 284:18244-18251.

11.   Rovner, A. S., P. M. Fagnant, and K. M. Trybus. 2006. Phosphorylation of a single head of smooth muscle myosin activates the whole molecule. Biochemistry 45:5280-5289.

12.   Trybus, K. M., T. W. Huiatt, and S. Lowey. 1982. A bent monomeric conformation of myosin from smooth muscle. Proc Natl Acad Sci U S A 79:6151-6155.

13.   Trybus, K. M., and S. Lowey. 1984. Conformational states of smooth muscle myosin. Effects of light chain phosphorylation and ionic strength. J Biol Chem 259:8564-8571.

14.   Milton, D. L., A. N. Schneck, D. A. Ziech, M. Ba, K. C. Facemyer, A. J. Halayko, J. E. Baker, W. T. Gerthoffer, and C. R. Cremo. Direct evidence for functional smooth muscle myosin II in the 10S self-inhibited monomeric conformation in airway smooth muscle cells. Proc Natl Acad Sci U S A 108:1421-1426.

15.   Koenderink, G. H., Z. Dogic, F. Nakamura, P. M. Bendix, F. C. MacKintosh, J. H. Hartwig, T. P. Stossel, and D. A. Weitz. 2009. An active biopolymer network controlled by molecular motors. Proc. Natl. Acad. Sci. U.S.A. 106:15192-15197.

16.   Janson, L. W., J. Kolega, and D. L. Taylor. 1991. Modulation of contraction by gelation/solation in a reconstituted motile model. J. Cell Biol. 114:1005-1015.

17.   Xu, J. Q., B. A. Harder, P. Uman, and R. Craig. 1996. Myosin filament structure in vertebrate smooth muscle. J Cell Biol 134:53-66.

Supplementary Movies:

Movie S1: F-actin asters. Time-lapse movie of fluorescent phalloidin images (inverted contrast) showing the F-actin "asters", which consist of F-actin with one end bound to neutravidin bead with the other filament end free to fluctuate. Time is indicated in seconds. Scale bar is 10 μm.

Movie S2: Formation of actomyosin bundles. Time-lapse movie of fluorescent myosin (inverted contrast) showing assembly of actomyosin bundles, with elapsed time indicated in minutes. Movie starts approximately 2 minutes after 1 μM myosin is introduced to the flow cell containing F-actin asters. Asterisks indicates bundle that appears to fall out of solution to become tethered near the surface. Arrow indicates a bundle formed by attachment of two asters. There is a focal drift occurring over the 23 minute movie. Scale bar is 10 μm.

Movie S3: Actomyosin bundle disintegration after ATP addition. Time-lapse movie of fluorescent myosin and phalloidin (inverted contrast) showing disintegration of actomyosin bundles after addition of 1 mM ATP at time = 0 s. Data obtained from bundles with 10% myosin saturation. Scale bar is 5 μm.

Movie S4: Stable, but non-contracting actomyosin bundle after ATP addition. Time-lapse movie of fluorescent myosin (inverted contrast) showing a stable, but non-contracting actomyosin bundles after addition of 1 mM ATP at time = 0 s. Data obtained from actomyosin bundles with 28% myosin saturation. Scale bar is 5 μm.

Move S5: Contracting actomyosin bundles after ATP addition. Time-lapse movie of fluorescent myosin (inverted contrast) showing contracting actomyosin bundles after addition of 0.1 mM ATP at time = 0 s. Data obtained from actomyosin bundles with 100% myosin saturation. Scale bar is 10 μm.

Movie S6: Contracting actomyosin bundle. Time-lapse movie of fluorescent myosin images (inverted contrast) shown in Fig. 2e. Contraction is initiated by addition of 0.1 mM ATP at time = 0 s. Data shown obtained from a region of the movie shown in Movie S5 of actomyosin bundles with 100% myosin saturation. Scale bar is 5 μm.

Move S7: Contraction generates tensile force. Time-lapse movie of fluorescent myosin images (inverted contrast) shown in Fig. 3b of a contracting actomyosin bundle with 100% myosin saturation and tethered to beads bound to the surface of a soft hydrogel. Contraction is initiated by addition of 1 mM ATP at time = 0 s. Red circles indicate initial positions of beads prior to contraction. Scale bar is 5 μm.